

Greenland climate would yield differences between ^{10}Be -derived and measured $\Delta^{14}\text{C}$. However, ^{14}C and ^{10}Be measurements with a better time resolution are necessary to correlate production-rate changes of these radionuclides on shorter timescales. During shorter but stable climate periods, when system changes can be excluded, we could even detect similarities in the fine structure of the two records.

^{10}Be in ice cores provides an independent tool to check the dating of ^{14}C time series older than 11,500 yr; this should allow various ^{14}C data sets to be synchronized, thus allowing a reliable extension of the tree-ring calibration curve. Additionally, high-resolution ^{10}Be data sets from other ice cores (for example, from Antarctica) could help to correct for potential transport effects on the ^{10}Be flux, and to establish a detailed production history of cosmogenic nuclides. The ^{10}Be -derived ^{14}C production rate can help in obtaining a consistent picture of the climate changes that occurred during the last deglaciation and of the role played by global deep-water formation in causing these changes. □

Received 9 March; accepted 17 October 2000.

- Siegenthaler, U., Heimann, M. & Oeschger, H. ^{14}C variations caused by changes in the global carbon cycle. *Radiocarbon* **22**, 177–191 (1980).
- Lal, D. & Peters, B. in *Handbuch für Physik* (ed. Flüge, S.) 551–612 (Springer, Berlin, 1967).
- Goslar, T., Arnold, M., Tisnerat-Laborde, N., Czernik, J. & Więckowski, K. Variations of Younger Dryas atmospheric radiocarbon explicable without ocean circulation changes. *Nature* **403**, 877–880 (2000).
- Hughen, K. *et al.* Deglacial changes in ocean circulation from an extended radiocarbon calibration. *Nature* **391**, 65–68 (1998).
- Finkel, R. C. & Nishiizumi, K. Beryllium 10 concentrations in the Greenland Ice Sheet Project 2 ice core from 3–40 ka. *J. Geophys. Res.* **102**, 26699–26706 (1997).
- Goslar, T. *et al.* High concentration of atmospheric ^{14}C during the Younger Dryas cold episode. *Nature* **377**, 414–417 (1995).
- Björck, S. *et al.* Synchronized terrestrial-atmospheric deglacial records around the North Atlantic. *Science* **274**, 1155–1160 (1996).
- Stocker, T. F. & Wright, D. G. Rapid changes in ocean circulation and atmospheric radiocarbon. *Paleoceanography* **11**, 773–795 (1996).
- Marchal, O. *et al.* Modelling the concentration of atmospheric CO_2 during the Younger Dryas climate event. *Clim. Dyn.* **15**, 341–354 (1999).
- Stuiver, M. & Polach, H. A. Discussion reporting of ^{14}C data. *Radiocarbon* **19**, 355–363 (1977).
- Beer, J. *et al.* Information on past solar activity and geomagnetism from ^{10}Be in the Camp Century ice core. *Nature* **331**, 675–679 (1988).
- Masarik, J. & Beer, J. Simulation of particle fluxes and cosmogenic nuclide production in the Earth's atmosphere. *J. Geophys. Res.* **104**, 12099–12111 (1999).
- McHargue, L. R. & Damon, P. E. The global beryllium-10 cycle. *Rev. Geophys.* **29**, 141–158 (1991).
- Broecker, W. S., Peteet, D. M. & Rind, D. Does the ocean–atmosphere system have more than one stable mode of operation? *Nature* **315**, 21–26 (1985).
- Wagner, G. Die kosmogenen Radionuklide ^{10}Be und ^{36}Cl im Summit-GRIP-Eisbohrkern. Thesis, ETH Zürich (1998).
- Wagner, G. *et al.* Chlorine-36 evidence for the Mono Lake event in the Summit GRIP ice core. *Earth Planet. Sci. Lett.* **181**, 1–6 (2000).
- Johnsen, S. J., Dansgaard, W. & White, J. W. C. The origin of Arctic precipitation under present and glacial conditions. *Tellus B* **41**, 452–468 (1989).
- Charles, C. D., Rind, D., Jouzel, J., Koster, R. D. & Fairbanks, R. G. Glacial-interglacial changes in moisture sources for Greenland: Influences on the ice core record of climate. *Science* **263**, 508–511 (1994).
- Siegenthaler, U. Uptake of excess CO_2 by an outcrop-diffusion model of the ocean. *J. Geophys. Res.* **88**, 3599–3608 (1983).
- Stuiver, M. *et al.* INTCAL98 radiocarbon age calibration, 24,000–0 cal BP. *Radiocarbon* **40**, 1041–1083 (1998).
- Stuiver, M. & Quay, P. D. Changes in atmospheric carbon-14 attributed to a variable sun. *Science* **207**, 11–19 (1980).
- Björck, S. *et al.* High-resolution analyses of an early Holocene cooling event may imply solar forcing as an important climate trigger. *Geology* (submitted).
- Alley, R. B. *et al.* Visual-stratigraphic dating of the GISP2 ice core: Basis, reproducibility, and application. *J. Geophys. Res.* **102**, 26367–26381 (1997).
- Hughen, K. A., Overpeck, J. T., Peterson, L. C. & Trumbore, S. Rapid climate changes in the tropical Atlantic region during the last deglaciation. *Nature* **380**, 51–54 (1996).
- Tauxe, L. Sedimentary records of relative paleointensity of the geomagnetic field: theory and practice. *Rev. Geophys.* **31**, 319–354 (1993).
- Alley, R. B. *et al.* Changes in continental and sea-salt atmospheric loadings in central Greenland during the most recent deglaciation: model-based estimates. *J. Glaciol.* **41**, 503–514 (1995).
- Johnsen, S. J., Dahl-Jensen, D., Dansgaard, W. & Gundestrup, N. Greenland palaeotemperatures derived from GRIP bore hole temperature and ice core isotope profiles. *Tellus B* **47**, 624–629 (1995).
- Johnsen, S. J. *et al.* Irregular glacial interstadials recorded in a new Greenland ice core. *Nature* **359**, 311–313 (1992).
- Johnsen, S. J. *et al.* The $\delta^{18}\text{O}$ record along the Greenland Ice Core Project deep ice core and the problem of possible Eemian climatic instability. *J. Geophys. Res.* **102**, 26397–26410 (1997).

30. Grootes, P. M. & Stuiver, M. Oxygen 18/16 variability in Greenland snow and ice with 10^{-3} - to 10^5 -year time resolution. *J. Geophys. Res.* **102**, 26455–26470 (1997).

Acknowledgements

Data were provided by the National Snow and Ice Data Center, University of Colorado at Boulder, and the WDC-A for Paleoclimatology, National Geophysical Data Center, Boulder, Colorado. We thank K. Hughen for the ^{14}C calibration data and the grey scale record of the Cariaco sediments. This work was supported by the Swiss National Science Foundation and the US Department of Energy.

Correspondence and requests for materials should be addressed to R.M. (e-mail: muscheler@eawag.ch).

Triggering of earthquake aftershocks by dynamic stresses

Deborah Kilb*†, Joan Gomberg‡ & Paul Bodin*

* Center for Earthquake Research and Information, The University of Memphis, 3876 Central Avenue, Suite 1, Memphis, Tennessee, 38152, USA

‡ US Geological Survey, Center for Earthquake Research and Information, 3876 Central Avenue, Suite 2, Memphis, Tennessee, 38152, USA

† Present address: Department of Geosciences, Princeton University, Princeton, New Jersey, USA.

It is thought that small ‘static’ stress changes due to permanent fault displacement can alter the likelihood of, or trigger, earthquakes on nearby faults¹. Many studies of triggering in the near-field, particularly of aftershocks, rely on these static changes as the triggering agent^{2–4} and consider them only in terms of equivalent changes in the applied load on the fault^{3–6}. Here we report a comparison of the aftershock pattern of the moment magnitude

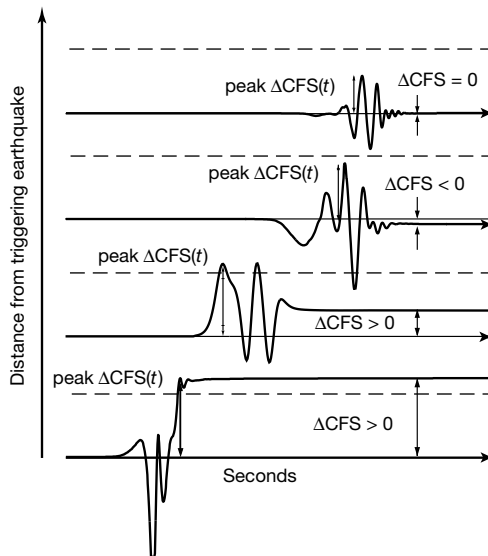


Figure 1 Cartoon time-histories of complete Coulomb stress change, $\Delta\text{CFS}(t)$, and its variation with distance. $\Delta\text{CFS}(t) = \Delta\tau(t) + \mu(\Delta\sigma(t) - B\Delta\rho(t))$ where $\Delta\tau$ and $\Delta\sigma$ denote changes in shear and normal stresses resolved on a fault plane, μ is the coefficient of friction, $\Delta\rho$ is the change in isotropic compressional stress, and B is similar to Skempton’s coefficient¹. Double arrows show peak $\Delta\text{CFS}(t)$ and static ΔCFS measurements. Dashed lines indicate hypothetical stress change threshold; peak $\Delta\text{CFS}(t)$ exceeds this threshold at the two close sites whereas the static Coulomb stress change exceeds it only at the closest site. ΔCFS thresholds are typically several per cent or less of the stress relieved by an earthquake¹.

$M_w = 7.3$ Landers earthquake, not only with static stress changes but also with transient, oscillatory stress changes transmitted as seismic waves (that is, 'dynamic' stresses). Dynamic stresses do not permanently change the applied load and thus can trigger earthquakes only by altering the mechanical state or properties of the fault zone. These dynamically weakened faults may fail after the seismic waves have passed by, and might even cause earthquakes that would not otherwise have occurred. We find similar asymmetries in the aftershock and dynamic stress patterns, the latter being due to rupture propagation, whereas the static stress changes lack this asymmetry. Previous studies have shown that dynamic stresses can promote failure at remote distances⁷⁻¹², but here we show that they can also do so nearby.

Earthquake-generated stress changes may enhance (or diminish) the tectonic load applied to another fault, moving it closer to (or further from) failure. Most studies have looked at permanent

changes in a linear combination of stress components known as the static Coulomb failure stress change (ΔCFS). ΔCFS may advance (or retard) failure by the approximate time required to accumulate an equivalent load at the tectonic loading rate. These times are often referred to as clock-advances (or clock-delays). Presumably earthquakes triggered by a clock-advance would have taken place at some later date.

Earthquakes also radiate seismic waves, which transmit transient, oscillatory stresses that do not permanently alter the net load on a fault. However, both dynamic and static stress changes may modify the properties of the fault zone itself, effectively changing the failure criteria¹³ and/or the nature and rates of mechanical or chemical processes that lead to earthquake rupture. Changes in the mechanical properties or failure processes of a fault do not mean that failure occurs immediately or with constant clock-advance; thus they allow variable time delays between triggering and triggered earthquakes.

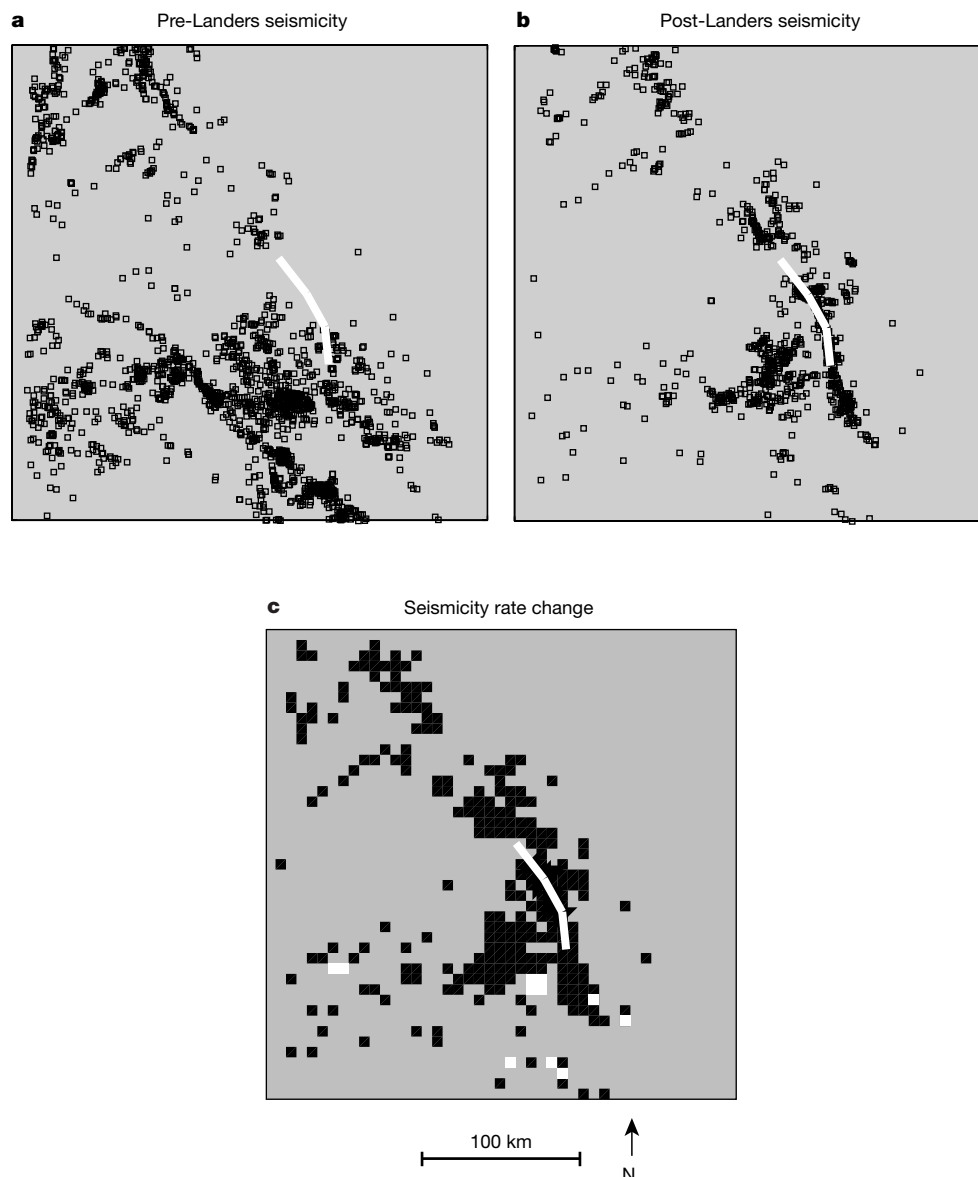


Figure 2 Pre- and post-Landers seismicity and calculated seismicity rate change. The regions of increased seismicity rate are very asymmetrically distributed about the Landers rupture (thick white line), with most of the increases occurring to the northwest. Maps of epicentres (squares) from 7/84 to 4/92 (**a**) and from 6/92 to 3/93 (**b**). This earlier background period is free of magnitude $M > 6$ events, significant network changes, and recording gaps. Catalogue completeness is assured by including only events of $M \geq 2.2$. Use of a declustered catalogue helps satisfy the assumption of independence between

earthquakes (other than with the Landers mainshock)²⁴⁻²⁵. **c**, Seismicity rate change map derived using a modified β -statistic²¹⁻²² which measures the difference between the observed number of post-Landers events in a grid cell and the number expected based on an average seismicity rate determined using the entire event population. Normalization of the difference by the standard deviation of the seismicity rate accounts for natural rate fluctuations. Black indicates increased rate, white decreased rate, and grey no rate change.

The delayed failure observed in aftershock sequences has been explained in terms of an approximate rate-state frictional-instability model and triggering by static stress changes². However, this same frictional model driven by dynamic stresses does not predict the delays required to generate an aftershock sequence, perhaps because it assumes fixed constitutive properties and/or that aftershocks are inevitable clock-advanced events. Thus, dynamic stress triggering may imply that aftershocks would never have occurred in the absence of the mainshock, being instead triggered by a change in the state of faults. Despite the difficulty of testing this idea, a few field observations¹² and theoretical models^{14,15} suggest that transient stresses may generate new earthquake-nucleating instabilities.

Transient and static changes are inseparable temporally (Fig. 1) so we refer to the ‘complete’ Coulomb stress change, denoted as $\Delta\text{CFS}(t)$. We propose that positive (in the direction of tectonic loading) maximum or peak values of $\Delta\text{CFS}(t)$, which occur during the transient stress changes and may include some component of static stress change, should correlate with increases in seismicity rate following a triggering earthquake. Sufficiently large positive stress changes may greatly alter and weaken faults, enhancing their likelihood of failure. Although the specific mechanisms that lead to instability and earthquake nucleation on crustal faults remain conjectural and are not addressed here, it is reasonable to assume that transient shear stresses cause irreversible weakening. For example, strengthening processes such as crack healing are too slow to counteract the effects of mechanisms such as sub-critical crack growth¹⁶. Also, if nucleation occurs as frictional instability governed by commonly assumed rate-state constitutive laws², then a rapid positive stress change weakens a fault much more than the strengthening that may occur owing to a rapid stress change of equal amplitude but opposite sign¹⁵. Laboratory data addressing differences between static and dynamic stresses on fault strength are scant, and one recent experiment shows that normal stress vibrations could lead to weakening or strengthening¹⁷. We employ earthquake data and theoretical calculations of stress changes, and ask what changes in the dynamic and static Coulomb stress are necessary to trigger observed seismicity rate changes. We do not expect peak $\Delta\text{CFS}(t)$ to lead to seismicity decreases.

Permanent positive and negative changes in the loading bring a fault closer to or further from failure, respectively, so we expect that the sign of ΔCFS should correlate with increases (positive) and decreases (negative) in seismicity rates. ΔCFS may also alter and weaken faults, but we discount this possibility because of its relatively much smaller amplitude (see below). We expect any correlation between $\Delta\text{CFS}(t)$ and seismicity rate changes to be imperfect, because other processes and factors undoubtedly also influence seismicity rates⁹. The Landers earthquake sequence in California is ideal for testing these hypotheses because the mainshock has a relatively simple and well-constrained source mechanism^{18,19}, and took place in a relatively well-instrumented region²⁰. One study of the Landers earthquake documents a strong correlation between ΔCFS and the spatial distribution of its aftershocks⁴. A similar correlation might reasonably exist with peak $\Delta\text{CFS}(t)$, because it usually exceeds ΔCFS . Beyond about 10 km from the causative rupture, peak $\Delta\text{CFS}(t)$ is typically more than an order of magnitude larger than ΔCFS .

We derive a map of seismicity rate change attributable to the Landers earthquake using the Southern California Seismic Network (SCSN) earthquake catalogue. We spatially grid the catalogued epicentres and compute the seismicity rate change in each grid cell using a modified version of the β -statistic^{21,22}. We assume a rate change is significant when $|\beta| \geq 1$ which, for a Poisson process, would be significant only at the 65% level. This choice of criterion compensates somewhat for the fact that seismicity is not poissonian, and for the effect of gridding the area, which causes the estimated rate change to appear more variable than both our intuition and the $\Delta\text{CFS}(t)$ maps suggest is appropriate. To avoid making unwarranted assumptions about the magnitude of the rate change and its relationship to $\Delta\text{CFS}(t)$, we assign rate increases, no rate change, and rate decreases values of 1, 0, and -1, respectively (Fig. 2).

We calculate $\Delta\text{CFS}(t)$ using a discrete-wavenumber reflectivity program²³. We constrain model parameters by modelling the Landers’ mainshock seismic displacements recorded at nearby broadband TERRAScope stations, and assuming that parameters that control surface displacements also control $\Delta\text{CFS}(t)$ at depth. The correlation between maps of Coulomb stress change and

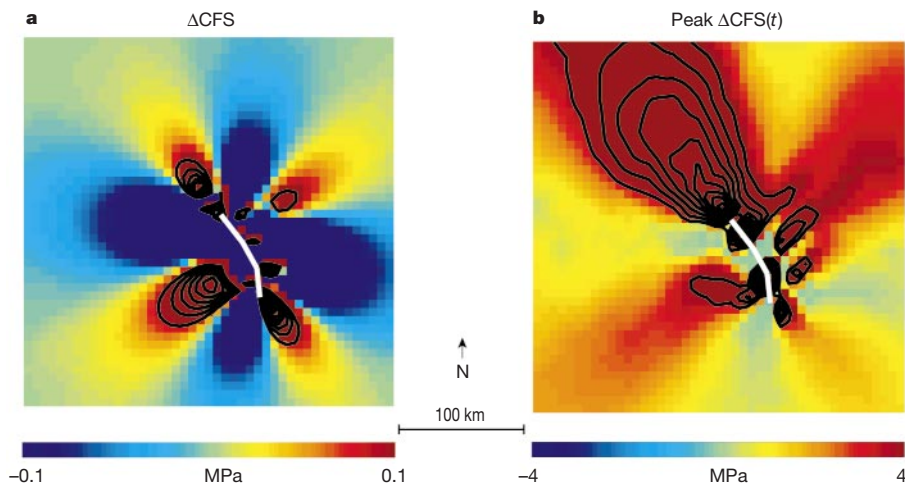


Figure 3 Maps of modelled ΔCFS and peak $\Delta\text{CFS}(t)$. Notable differences between these maps are the greater asymmetry about the Landers rupture (white lines) and much larger amplitudes in the peak $\Delta\text{CFS}(t)$ map. The amplitude scales are chosen to optimize the correlation with the seismicity rate change (see text). Calculations require resolving the stress field on the fault planes of the triggered events. We chose mean values of strongly peaked histograms of aftershock focal mechanism parameters and depths reported in the SCSN catalogue as the most appropriate (strike, 330°; dip, 90°; rake, 180°; depth, 4.5 km). This fault plane is also nearly optimally oriented given the regional stress field and approximately parallels the general strike of mapped faults. Positive $\Delta\text{CFS}(t)$ is that which would produce slip in the observed rake direction. We assume Coulomb parameters (see

Fig. 1 legend) of $\mu = 0.6$ and $B = 0.85$, in accord with previous studies of ΔCFS ¹. **a**, ΔCFS map contoured at intervals of 0.05 MPa for values ≥ 0.1 MPa and shaded for smaller values. The addition of the $M = 6.1$ Joshua Tree and $M = 6.5$ Big Bear earthquakes to the stress calculations causes the high positive stress lobes in the southwest and southeast to become slightly more heterogeneous (that is, mixed with small regions of negative stress change). **b**, Peak $\Delta\text{CFS}(t)$ map contoured at intervals of 1.5 MPa for values ≥ 4 MPa and shaded for smaller values. Addition of the Joshua Tree and Big Bear earthquakes causes the high in the southwest to elongate southwesterly by a few tens of kilometres.

seismicity rate change depends on the range of stress change values considered significant. For peak $\Delta\text{CFS}(t)$ and for $|\Delta\text{CFS}|$ we search for the minimum value, or threshold, that optimizes the correlation (that is, the smallest contour levels in Fig. 3a and b). We interpret this as constraining the stress change threshold (assumed here to be regionally uniform) required to alter the fault rheology or the load enough to change the failure rate. For a given threshold, if the extreme values of peak $\Delta\text{CFS}(t)$ or ΔCFS in each cell exceed the threshold the cell is assigned a value of 1, if the extreme value is below the negative of the threshold it is assigned a value of -1 , and all others are assigned zeros.

We measure the correlation by counting the number of grid cells in which both the Coulomb stress and seismicity rate changes match. Allowing for the possibility that a rate decrease has gone undetected in regions of low rates, owing to our short observation period, we also increment the count for grid cells in which ΔCFS equals -1 and the seismicity rate change is zero as a result of no pre- and post-Landers seismicity. The significance of the correlation count for each threshold tested is estimated by comparing it to the statistical distribution of counts obtained by repeating the procedure 500 times, using spatially randomized seismicity rate change

maps. Significant counts, or correlations, must differ from the mean of the randomized counts by two or more standard deviations and the optimal threshold produces the most significant correlation. The optimal triggering thresholds at a depth of 4.5 km, corresponding to the mean aftershock depth, equal 0.1 MPa for ΔCFS (Fig. 3a) and 4.0 MPa for peak $\Delta\text{CFS}(t)$ (Fig. 3b). This static threshold is consistent with that found in other studies^{1,3}. Significant correlations exist for thresholds of 0.001 to 0.5 MPa for ΔCFS and more than 0.5 MPa for peak $\Delta\text{CFS}(t)$. We also computed maps of ΔCFS and peak $\Delta\text{CFS}(t)$ at the surface, and at depths of 2 km and 11 km. Although the absolute amplitudes of ΔCFS and peak $\Delta\text{CFS}(t)$ decrease slightly with depth, the mapped patterns do not change significantly. Correlation results are similarly robust with respect to plausible variations in the assumed geometry of aftershock fault planes.

Both ΔCFS and peak $\Delta\text{CFS}(t)$ correlate statistically with seismicity rate change with a high degree of confidence (well outside the tails of the distribution of random correlations). Despite this high confidence, our statistical method suggests that both ΔCFS and peak $\Delta\text{CFS}(t)$ predict seismicity rate changes no more than 7% better than a random process. However, a qualitative visual assessment of the correlations (Fig. 4) indicates that this is clearly overly conservative, because the eye smooths the seismicity rate change maps more in accord with the variability of the stress changes than does our statistical measure. Because earthquakes are represented as point data, the β -statistic depends strongly on grid cell size. The $6 \times 6 \text{ km}^2$ cell size was chosen to capture accurately the fluctuation in stress changes close to the mainshock fault, and whereas the statistical correlations could be enhanced if we increased our cell size or applied a smoothing operator, it is not clear how to do this objectively.

Statistically ΔCFS and peak $\Delta\text{CFS}(t)$ correlate with seismicity rate change equally well. At the closest distances, only an amplitude scaling relationship differs between the two. Farther out the asymmetry in the aftershock distribution correlates better with the asymmetry in the peak $\Delta\text{CFS}(t)$ map, which is absent in the ΔCFS map. The peak $\Delta\text{CFS}(t)$ asymmetry results from the mainshock's unilateral northward rupture propagation, and its correlation with the aftershock pattern leaves little doubt that the peak stresses, although transient, exert a controlling influence. Even our more conservative statistical results imply that the many previous studies that suggest a causal relationship between ΔCFS and seismicity rate change^{3,22} may be missing an important part of the triggering process. Moreover, we expect dynamic stresses, thanks to their much larger amplitude relative to the static changes, to alter fault zone properties more effectively in ways that permit a range of time-delays between triggering and triggered events. Permanent stress changes can also contribute to the alteration of fault zone properties, but our results indicate that this effect may be relevant only extremely close to the mainshock rupture where the permanent stress changes may be nearly as large as the dynamic stresses. Preliminary analyses of the moment magnitude $M_w = 7.1$ Hector Mine, California earthquake of 16 October 1999 also show a strong correlation between its rupture dynamics (directivity direction) and the change in seismicity rate at remote distances. Although the existence of a similar correlation in the near-field remains to be determined, these preliminary results suggest that nature may have just reconfirmed the lessons offered by the Landers earthquake. \square

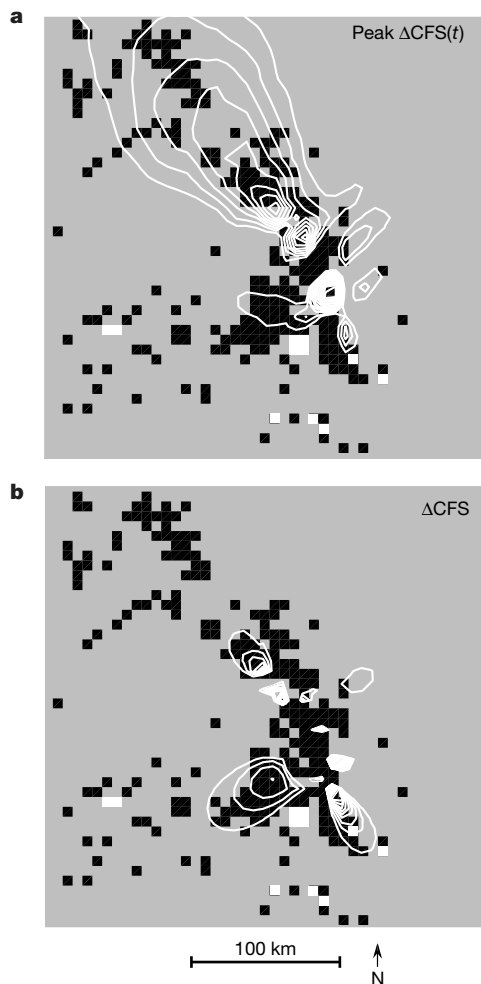


Figure 4 Comparisons of peak $\Delta\text{CFS}(t)$ and ΔCFS with seismicity rate change. The peak $\Delta\text{CFS}(t)$ contours and the pattern of seismicity rate change share the same asymmetry, which is lacking in the ΔCFS contours. Contours (from Fig. 3) show (a) peak $\Delta\text{CFS}(t) \geq 4 \text{ MPa}$ (interval, 1.5 MPa) and (b) $\Delta\text{CFS} \geq 0.1 \text{ MPa}$ (interval, 0.05 MPa). Map shading indicates significant rate increases (black), decreases (white) and regions of no change (grey). The correlation of seismicity rate change with peak $\Delta\text{CFS}(t)$ improves slightly with the addition of the $M = 6.1$ Joshua Tree and $M = 6.5$ Big Bear earthquakes to the stress calculations, and has negligible effect on the correlation with ΔCFS .

Received 10 January; accepted 28 August 2000.

- Harris, R. A. Introduction to special section: Stress triggers, stress shadows, and implications for seismic hazard. *J. Geophys. Res.* **103**, 24347–24358 (1998).
- Dieterich, J. A. A constitutive law for rate of earthquake production and its application to earthquake clustering. *J. Geophys. Res.* **99**, 2601–2618 (1994).
- Toda, S., Stein, R. S., Reasenberg, P. A., Dieterich, J. & Yoshida, A. Stress transferred by the 1995 Mw=6.9 Kobe, Japan shock: Effect on aftershocks and future earthquake probabilities. *J. Geophys. Res.* **103**, 24543–24566 (1998).
- King, G. C. P., Stein, R. S. & Lin, J. Static stress changes and the triggering of earthquakes. *Bull. Seismol. Soc. Am.* **84**, 935–953 (1994).

5. Jaume, S. C. & Sykes, L. R. Changes in state of stress on the southern San Andreas Fault resulting from the California earthquake sequence of April to June, 1992. *Science* **258**, 1325–1328 (1992).
6. Harris, R. A. & Simpson, R. W. Changes in static stress on southern California faults after the 1992 Landers earthquake. *Nature* **360**, 251–254 (1992).
7. Anderson, J. G. *et al.* Seismicity in the western Great Basin apparently triggered by the Landers, California, earthquake, 28 June 1992. *Bull. Seismol. Soc. Am.* **84**, 863–891 (1994).
8. Gomberg, J. & Bodin, P. Triggering of the Little Skull Mountain, Nevada earthquake with dynamic strains. *Bull. Seismol. Soc. Am.* **84**, 844–853 (1994).
9. Gomberg, J. Stress/strain changes and triggered seismicity following the Ms7.3 Landers, California, earthquake. *J. Geophys. Res.* **101**, 751–764 (1996).
10. Gomberg, J. & Davis, S. Stress/strain changes and triggered seismicity at The Geysers, California. *J. Geophys. Res.* **101**, 733–749 (1996).
11. Hill, D. P. *et al.* Seismicity remotely triggered by the magnitude 7.3 Landers, California, earthquake. *Science* **260**, 1617–1623 (1993).
12. Hill, D. P., Johnston, M. J. S., Langbein, J. O. & Bilham, R. Response of Long Valley caldera to the Mw=7.3 Landers, California, earthquake. *J. Geophys. Res.* **100**, 12985–13005 (1995).
13. Gomberg, J., Beeler, N. M., Blanpied, M. L. & Bodin, P. Earthquake triggering by transient and static deformations. *J. Geophys. Res.* **103**, 24411–24426 (1998).
14. Boatwright, J. & Cocco, M. Frictional constraints on crustal faulting. *J. Geophys. Res.* **101**, 13895–13909 (1996).
15. Gomberg, J., Blanpied, M. L. & Beeler, N. M. Transient triggering of near and distant earthquakes. *Bull. Seismol. Soc. Am.* **87**, 294–309 (1997).
16. Atkinson, B. K. Subcritical crack growth in geologic materials. *J. Geophys. Res.* **89**, 4077–4114 (1984).
17. Richardson, E. & Marone, C. Effects of normal stress vibrations on frictional healing. *J. Geophys. Res.* **104**, 28857–28878 (1999).
18. Dreger, D. S. Investigation of the rupture process of the 28 June 1992 Landers earthquake utilizing TERRAScope. *Bull. Seismol. Soc. Am.* **84**, 713–724 (1994).
19. Wald, D. J. & Heaton, T. H. Spatial and temporal distribution of slip for the 1992 Landers, California, earthquake. *Bull. Seismol. Soc. Am.* **84**, 668–691 (1994).
20. Hauksson, E., Jones, L. M., Hutton, K. & Eberhart-Phillips, D. The 1992 Landers earthquake sequence: seismological observations. *J. Geophys. Res.* **98**, 19835–19858 (1993).
21. Matthews, M. V. & Reasenberg, P. A. Statistical methods for investigating quiescence and other temporal seismicity patterns. *Pure Appl. Geophys.* **126**, 357–372 (1988).
22. Reasenberg, P. A. & Simpson, R. W. Response of regional seismicity to the static stress change produced by the Loma Prieta earthquake. *Science* **255**, 1687–1690 (1992).
23. Cotton, F. & Coutant, O. Dynamic stress variations due to shear faults in a plane-layered medium. *Geophys. J. Int.* **128**, 676–688 (1997).
24. Frohlich, C. & Davis, S. D. Single-link cluster analysis as a method to evaluate spatial and temporal properties of earthquake catalogs. *Geophys. J. Int.* **100**, 19–32 (1990).
25. Davis, S. D. & Frohlich, C. Single-link cluster analysis of earthquake aftershocks: decay laws and regional variations. *J. Geophys. Res.* **96**, 6335–6350 (1991).

Acknowledgements

We are grateful to F. Cotton, O. Coutant, P. Reasenberg and S. Davis for kindly supplying us with their computer codes. We thank S. Hough, M. Johnston & C. Marone for thoughtful reviews. The US Geological Survey funded this work.

Correspondence and requests for materials should be addressed to J.G. (e-mail: gomberg@usgs.gov).

Geochemical evidence for terrestrial ecosystems 2.6 billion years ago

Yumiko Watanabe*†, Jacques E. J. Martini‡ & Hiroshi Ohmoto*

*Astrobiology Research Center and Department of Geosciences, The Pennsylvania State University, University Park, Pennsylvania 16802, USA

†Faculty of Science, Tohoku University, Sendai, 980-8578, Japan

‡Geological Survey of South Africa, Private Bag X112, Pretoria, South Africa

Microorganisms have flourished in the oceans since at least 3.8 billion years (3.8 Gyr) ago^{1,2}, but it is not at present clear when they first colonized the land. Organic matter in some Au/U-rich conglomerates and ancient soils of 2.3–2.7 Gyr age has been suggested as remnants of terrestrial organisms^{3–5}. Some 2.7-Gyr-old stromatolites have also been suggested as structures created by terrestrial organisms^{6–7}. However, it has been disputed whether this organic matter is indigenous or exogenic, and whether these stromatolites formed in marine or fresh water. Consequently, the oldest undisputed remnants of terrestrial organisms are currently the 1.2-Gyr-old microfossils from Arizona, USA⁸. Unusually carbonaceous ancient soils—palaeosols—have been found in

the Mpumalanga Province (Eastern Transvaal) of South Africa⁹. Here we report the occurrences, elemental ratios (C, H, N, P) and isotopic compositions of this organic matter and its host rocks. These data show that the organic matter very probably represents remnants of microbial mats that developed on the soil surface between 2.6 and 2.7 Gyr ago. This places the development of terrestrial biomass more than 1.4 billion years earlier than previously reported.

In the Mpumalanga Province of South Africa, many palaeosols have been recognized on the Archaean basement complex, which is composed primarily of granites, granite-gneisses, basalts and minor ultramafic rocks (for example, dunite, peridotite and serpentinite) of age 2.7–3.6 Gyr. These palaeosols are overlain by various formations of the Transvaal Supergroup (2.1–2.6 Gyr), and were subjected to the zeolite- to lower green-schist facies metamorphism (temperature $T < \sim 300^\circ\text{C}$) associated with the intrusion of the 2.05-Gyr Bushveld Igneous Complex (Fig. 1) (ref. 9). Palaeosols on granites and basalts often exceed 20 m in thickness. They are easily recognizable because of the abundant aluminosilicates (feldspars, biotite, hornblende) in the parental rocks that were converted to less-soluble, pale, Al_2O_3 -rich clays, such as kaolinite, smectite and sericite. In contrast, thick palaeosols rarely develop on ultramafic rocks because such rocks are mostly composed of aluminium-poor silicates (olivine, pyroxene) that are easily leached out by rain water. Exceptionally thick soils may develop on ultramafic rocks when the porous spaces created by dissolution of silicate minerals are continuously filled by aerosols or by precipitation of new minerals (for example, calcite, dolomite and silica) from soil water and/or ground water. Such palaeosols were discovered at Schagen, Elandshoek and Kalkkloof areas in Mpumalanga Province (Fig. 1) (ref. 9). The data we give here are from the organic matter at Schagen.

The palaeosol section at Schagen developed on a >2.7-Gyr serpentinitized dunite, and is overlain by a quartzite bed (~30-m thick) of the 2.6-Gyr Black Reef Formation. Therefore, the palaeosol

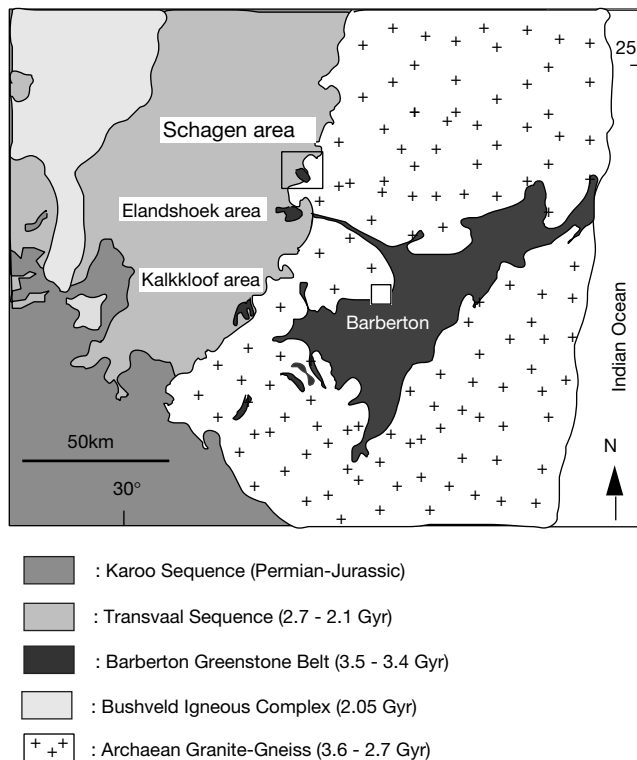


Figure 1 A simplified map of Mpumalanga Province, South Africa. The figure shows the main geological units, and the localities of organic-rich palaeosols (Schagen, Elandshoek, Kalkkloof) (modified after ref. 9).